Structural transition, ferro-orbital order and its fluctuation-mediated s_{++}-wave superconductivity in iron pnictides

Yoshiaki Ōno[a,b], Yuki Yanagi[a], Naoko Adachi[a], Youichi Yamakawa[a]

[a]*Department of Physics, Niigata University, Ikarashi, Niigata 950-2181, Japan*
[b]*JST, Transformative Research-Project on Iron Pnictides (TRIP), Chiyoda, Tokyo 102-0075, Japan*

Abstract

We investigate the electronic states and the superconductivity in the two-dimensional 16-band d-p model extracted from a tight-binding fit to the band structure of iron pnictides, in the presence of both the Coulomb interaction between Fe d-electrons and the electron-lattice coupling g with the orthorhombic mode which is crucial for reproducing the recently observed ultrasonic softening of the elastic constant C_{66}. Due to the cooperative effects of these interactions, the ferro-orbital order with different occupations of d_{yz} and d_{zx} orbitals occurs and induces the tetragonal-orthorhombic structural transition at T_s, together with the stripe-type antiferromagnetic (AFM) order below T_N. For a large g case, we obtain the phase diagram consistent with the doped iron pnictides with $T_s > T_N$ for $x > 0$, where the s_{++}-wave superconductivity is mediated by the ferro-orbital fluctuation which is largely enhanced near the ferro-orbital QCP at x_c with $T_s \to 0$. On the other hand, for a small g case, the simultaneous phase transition occurs at $T_s = T_N$ even for $x > 0$, where the $s_{\pm}$-wave superconductivity is mediated by the AFM fluctuation. Both the s-wave states with full superconducting gaps are consistent with most of the experiments but only the former is considered to account for the small T_c-suppression against nonmagnetic impurities.

Keywords: A. Superconductors; D. Electron-electron interactions; D. Electron-phonon interactions; D. Phase transitions

1. Introduction

The discovery of the iron pnictide superconductors RFePnO$_{1-x}$F$_x$ (R=Rare Earth, Pn=As, P) [1, 2] with a high transition temperature exceeding 50K [3] has triggered an intense research effort to search for new superconducting materials and to investigate the physical properties of these materials. The parent compounds with $x = 0$ show the tetragonal-orthorhombic structural transition and the stripe-type antiferromagnetic (AFM) transition. For example, LaFeAsO shows the structural phase transition at $T_s \sim 155$K from the tetragonal phase ($T > T_s$) to the orthorhombic phase ($T < T_s$) and the stripe-type AFM order below $T_N \sim 137$K with a magnetic moment $\sim 0.35\mu_B$ at low temperature [4, 5]. The carrier doping x suppresses both of the transition temperatures T_s and T_N and induces the superconductivity as shown in Fig. 1. Therefore, the magnetic order and/or the structural transition are considered to play important roles in the mechanism of the superconductivity.

When the carrier doping x is varied, T_s is found to be always higher than T_N in 1111 system such as RFeAsO$_{1-x}$F$_x$ [6, 7] and 111 system such as NaFe$_{1-x}$Co$_x$As [8], while in 122 system such as Ba(Fe$_{1-x}$Co$_x$)$_2$As$_2$ [9], the simultaneous first-order transition ($T_s = T_N$) for $x = 0$ is found to split into two second-order transitions ($T_s > T_N$) with doping x. In 11 system such as Fe$_{1-x}$Co$_x$Se$_{1-\delta}$ [10], the structural transition is observed without AFM transition. It should be stressed that the structural transition is a common feature of iron-based superconductors and T_s is always higher than T_N for doped iron pnictides.

As shown in Fig. 1, there are distinct three phases: the tetragonal phase for $T > T_s$, the orthorhombic phase with the stripe-type AFM for $T < T_N$, and the orthorhombic phase without the AFM for $T_N < T < T_s$. We note that the orthorhombic phase without the AFM should be called the monoclinic phase in the original unit cell shown in Fig. 1, but we called it the orthorhombic phase by using the magnetic unit cell below T_N for avoiding confusion. Both the transitions at T_s and T_N are the second-order as shown in the specific heat [11] and the neutron experiments [4]. In general, when the system approaches the second-order transition point, the fluctuation (the susceptibility) of the corresponding order parameter diverges and may be responsible for the pairing interaction for the superconductivity. As the orthorhombic phase without the AFM is next to the superconducting phase (see Fig. 1), the fluctuation which diverges towards T_s is considered to have most significant effect on the superconductivity.

Remarkably, drastic softening of the elastic constant C_{66} has been observed in recent ultrasonic experiments [11, 12, 13, 14]. The temperature dependence is well fitted by the expression, $C_{66} = C_{66}^0(T-T_s)/(T-\theta)$, where C_{66} becomes zero at the structural transition temperature T_s, and then shows divergent behavior towards a critical temperature θ [13, 14]. The systematic ultrasonic measurements in Ba(Fe$_{1-x}$Co$_x$)$_2$As$_2$ with various doping x [13] have revealed that, with increasing x, both of T_s and θ decrease with a huge Jahn-Teller energy given by $E_{JT} = T_s - \theta$ of ~ 50K or more, and T_s becomes zero at $x_c \sim 0.07$ where a
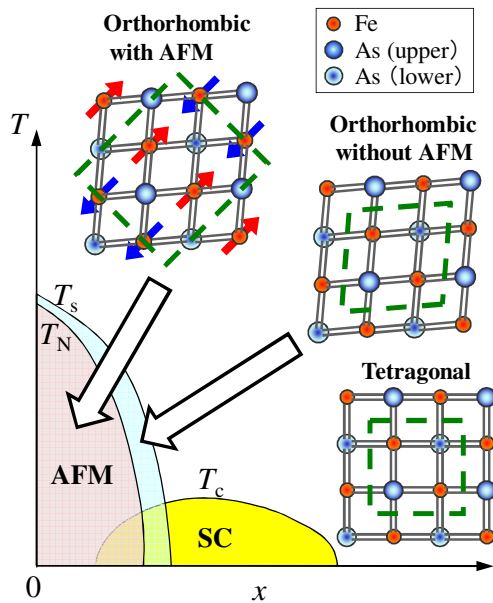
Figure 1: (Color online) Schematic phase diagram of iron pnictides as functions of the carrier doping x and the temperature T, where T_s, T_N and T_c are the transition temperatures for the tetragonal-orthorhombic structural transition, the stripe-type AFM transition and the superconducting transition, respectively. Dashed squares denote the unit cells of the corresponding three phases: the tetragonal phase, the orthorhombic phase with the stripe-type AFM (arrows show spins), and the orthorhombic phase without the AFM.

Figure 2: (Color online) Schematic figures of the strain fields for $C_E = (C_{11} - C_{12})/2$, C_{44} and C_{66} modes (a), (b) and (c), the orbital fluctuations coupled with the corresponding strain fields (d), (e) and (f), and the phonons for B_{1g}, E_g and orthorhombic modes which enhance the corresponding orbital fluctuations (g), (h) and (i), respectively. The x', y' (x, y) axes are directed along the nearest (second nearest) Fe-Fe bonds (reproduced from Ref. [15]).

quantum critical behavior is observed. For overdoped case with $x > x_c$, the system does not show the structural transition but still shows the drastic softening of C_{66} down to the superconducting transition temperature T_c below which C_{66} shows the hardening with a kink at T_c.

Generally, the elastic constant C_Γ is given by the second derivative of the Free energy w.r.t. the strain field ε_Γ induced by the ultrasound and includes the contribution such as $-g_\Gamma^2 \chi_{O_\Gamma}$ with the susceptibility χ_{O_Γ} for the electric quadrupole operator O_Γ linearly coupled with the strain field as $g_\Gamma O_\Gamma \varepsilon_\Gamma$. When the irreducible quadrupole susceptibility shows divergent behavior with a critical temperature θ as $\chi_{O_\Gamma} \sim A_\Gamma/(T - \theta)$, we obtain the expression for C_Γ mentioned in the preceding paragraph, where the Jahn-Teller energy is given by $E_{JT} = g_\Gamma^2 A_\Gamma/C_\Gamma^0$. Then, the enhancement of χ_{O_Γ} is responsible for the softening of C_Γ and the large value of E_{JT} indicates the presence of a large electron-lattice coupling g_Γ.

The detailed ultrasonic measurement in $Ba(Fe_{0.9}Co_{0.1})_2As_2$ [14] has revealed a significant selection rule where the softening is observed only for the elastic constant C_{66} while the other elastic constants C_{44} and $C_E = (C_{11} - C_{12})/2$ show no softening. In the case of C_{66}, the ultrasound introduces the strain field ε_{xy} which corresponds to the orthorhombic distortion and linearly couples to the quadrupole O_{xy} corresponding to the orbital fluctuations of the longitudinal $d_{y'z}$-$d_{zx'}$ and/or transverse $d_{3z^2-r^2}$-d_{xy} modes, where the x', y' (x, y) axes are directed along the nearest (second nearest) Fe-Fe bonds as shown in Fig. 2 [15] (see also Fig. 3). Therefore, the drastic softening of C_{66} indi-
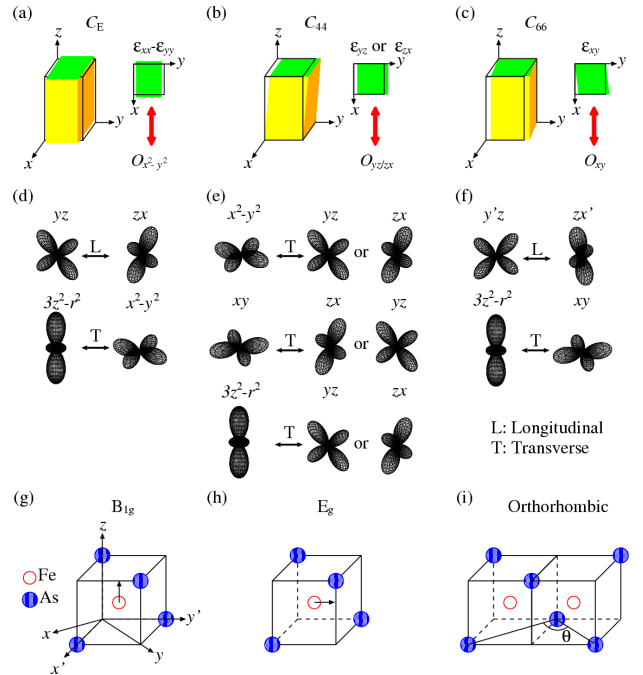
cates that the O_{xy} quadrupole susceptibility (the corresponding orbital susceptibilities) is largely enhanced at low temperature down to T_s and T_c, and there exists a large electron-lattice coupling g with the orthorhombic mode. Remarkably, the softening of C_{66} is found to be almost unchanged under the external magnetic fields up to 10T [14] and up to 60T in more recent experiments [16], indicating the nonmagnetic origin of the softening, in contrast to the nematic fluctuation mechanism [12] where the structural order and its fluctuation is induced by magnetic fluctuations.

Theoretically, the orthorhombic phase with the AFM was well described by first-principles calculations [17], where the stripe-type AFM is realized due to the effect of nesting between the hole and electron Fermi surfaces and induces different occupancy for the $y'z$ and zx' orbitals and therefore breaks the tetragonal symmetry resulting in the orthorhombic phase. The similar induced orbital order was also obtained by the Hartree-Fock calculations based on the multi-orbital Hubbard models [18, 19]. However, the orthorhombic phase without the AFM was not obtained there. The purpose of this paper is to present a theoretical description of the phase diagram of iron pnictides including the orthorhombic phase without the AFM, where the effect of the electron-lattice coupling with the orthorhombic mode, which is responsible for the softening of C_{66} with the large Jahn-Teller energy, is crucial for reproducing the phase diagram with $T_s > T_N$.

As for the superconductivity, the s-wave pairing with sign

change of the order parameter between the hole and electron Fermi surfaces, so called $s_\pm$-wave, mediated by the AFM fluctuation was proposed as a possible pairing state in the iron pnictides [20, 21, 22, 23, 24]. The $s_\pm$-wave state with a full superconducting gap seems to be consistent with most of the experiments [25]. As for the impurity effects, however, the small T_c-suppression against nonmagnetic impurities [26, 27] is not consistent with the $s_\pm$-wave state where T_c is considered to rapidly decrease with the nonmagnetic impurities [28]. Therefore, the s-wave state without sign change of the order parameter, so called s_{++}-wave, mediated by the orbital fluctuation which is enhanced due to the effects of the inter-orbital Coulomb interaction was proposed on the basis of the one-dimensional two-band Hubbard model [29, 30] and the two-dimensional 16-band d-p model [31].

The orbital fluctuation is known to be enhanced by the electron-phonon interaction in addition to the inter-orbital Coulomb interaction. Recently, the effects of the electron-phonon interaction with B_{1g} and E_g modes on the orbital fluctuation and its induced s_{++}-wave superconductivity have been investigated by Kontani and Onari [32] on the basis of the 5-band Hubbard model. We have also investigated the effects of the electron-phonon interaction with B_{1g}, E_g and A_{1g} modes on the basis of the 16-band d-p model [33]. As shown in Fig. 2, the B_{1g} phonon enhances the longitudinal d_{yz}-d_{zx} and transverse $d_{3z^2-r^2}$-$d_{x^2-y^2}$ orbital fluctuations responsible for the softening of C_E, while the E_g phonon enhances the transverse $d_{x^2-y^2}$-d_{yz}, d_{xy}-d_{zx} and $d_{3z^2-r^2}$-d_{yz} orbital fluctuations responsible for the softening of C_{44}.

More recently, we have also investigated the effect of the electron-phonon coupling g with the orthorhombic mode which enhances the longitudinal $d_{y'z}$-$d_{zx'}$ and transverse $d_{3z^2-r^2}$-d_{xy} orbital fluctuations (O_{xy} quadrupole fluctuation) responsible for the softening of C_{66} [15]. Due to the cooperative effect of the Coulomb and electron-phonon interactions, the system shows the ferro-orbital order which induces the tetragonal-orthorhombic structural transition at T_s, together with the stripe-type AFM order below T_N. Near the phase transitions, the s_{++}-wave superconductivity occurs due to the orbital fluctuation for a large g case with $T_s > T_N$, while the $s_\pm$-wave does due to the magnetic fluctuation for a small g case with $T_s = T_N$. The former case is consistent with the phase diagram of doped iron pnictides with $T_s > T_N$.

In this paper, we review our theoretical study on the electronic states and the superconductivity in iron pnictides based on the recent published work [15, 24, 31, 33, 34, 35], using a different parameter set. In addition, we present a more detailed analysis of the phase diagram and the ultrasonic softening. We first introduce our model Hamiltonian and formulation in Section 2. Then, we show the calculated results in Section 3. Finally, we summarize and discuss our findings in Section 4.

2. Model and formulation

First of all, we perform the density functional calculation for LaFeAsO with the generalized gradient approximation of
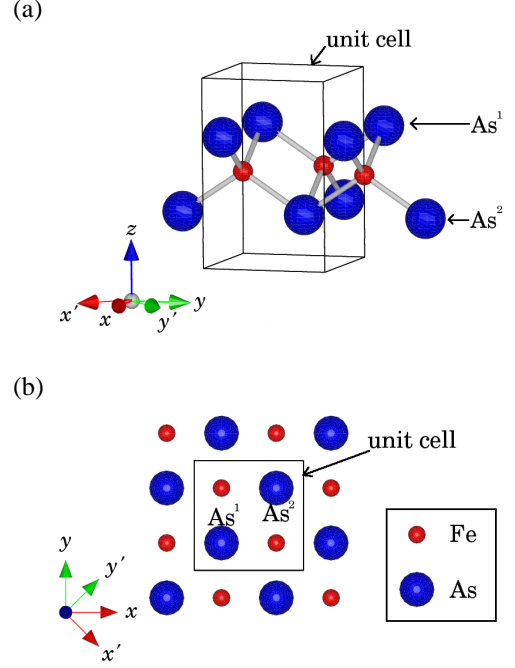

Figure 3: (Color online) Crystal structure of Fe_2As_2 layer. Small and large balls represent Fe and As atoms, respectively. The solid line represents the unit cell. It is noted that As^1 and As^2 denote the As atoms on the upper side and on the lower side of the Fe_2As_2 layer, respectively (reproduced from Ref. [31])

Perdew, Burke and Ernzerhof [36] by using the WIEN2k package [37], where the lattice parameters (a = 4.03268Å, c = 8.74111Å) and the internal coordinates (z_{La} = 0.14134, z_{As} = 0.65166) are experimentally determined [38]. The crystal structure of Fe_2As_2 layer is shown in Fig. 3 (a). Since As atoms are tetrahedrally arranged around a Fe atom, there are two distinct Fe and As sites in the crystallographic unit cell (see Figs. 3 (a), (b)). Considering these facts, we then derive the two-dimensional 16-band d-p model [24, 31], where $3d$ orbitals ($d_{3z^2-r^2}$, $d_{x^2-y^2}$, d_{xy}, d_{yz}, d_{zx}) of two Fe atoms (Fe^1=A, Fe^2=B) and $4p$ orbitals (p_x, p_y, p_z) of two As atoms are explicitly included. We note that the x', y' (x, y) axes are directed along the nearest (second nearest) Fe-Fe bonds as mentioned before. Hereafter, we number the Fe-$3d$ orbitals as follows: $d_{3z^2-r^2}$(1), $d_{x^2-y^2}$(2), d_{xy}(3), d_{yz}(4), d_{zx}(5).

The total Hamiltonian of the d-p model is given by

$$H = H_0 + H_{int} + H_{ph} + H_{el-ph}, \tag{1}$$

where H_0, H_{int}, H_{ph} and H_{el-ph} are the kinetic, Coulomb interaction, phonon and electron-phonon interaction parts of the Hamiltonian, respectively. The kinetic part of the Hamiltonian is given by the following tight-binding Hamiltonian,

$$
\begin{aligned}
H_0 &= \sum_{i,\ell,\sigma} \varepsilon_\ell^d d_{i\ell\sigma}^\dagger d_{i\ell\sigma} + \sum_{i,m,\sigma} \varepsilon_m^p p_{im\sigma}^\dagger p_{im\sigma} \\
&+ \sum_{i,j,\ell,\ell',\sigma} t_{i,j,\ell,\ell'}^{dd} d_{i\ell\sigma}^\dagger d_{j\ell'\sigma} + \sum_{i,j,m,m',\sigma} t_{i,j,m,m'}^{pp} p_{im\sigma}^\dagger p_{jm'\sigma} \\
&+ \sum_{i,j,\ell,m,\sigma} t_{i,j,\ell,m}^{dp} d_{i\ell\sigma}^\dagger p_{jm\sigma} + h.c.,
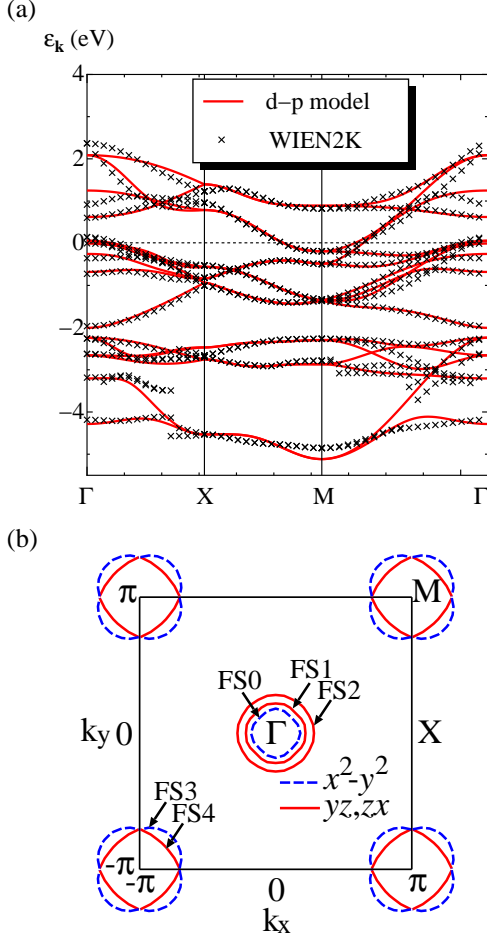\end{aligned} \tag{2}
$$

3

Figure 4: (Color online) (a) The band structure obtained from the *d-p* model eq. (2) (solid line) and that obtained from the density functional calculation (cross) for LaFeAsO, where the Fermi level is set to 0 on the energy axis. (b) The corresponding Fermi surface obtained from the *d-p* model. The solid and dashed lines show the Fermi surfaces where d_{yz}, d_{zx} and $d_{x^2-y^2}$ orbital characters are the most dominant, respectively.

$t^{dd}_{\alpha\ell,\beta\ell'}$	$Fe^1\ d_{3z^2-r^2}$	$Fe^1\ d_{x^2-y^2}$	$Fe^1\ d_{xy}$	$Fe^1\ d_{yz}$	$Fe^1\ d_{zx}$	$Fe^2\ d_{3z^2-r^2}$	$Fe^2\ d_{x^2-y^2}$	$Fe^2\ d_{xy}$
$Fe^1\ d_{3z^2-r^2}$	−0.024	−0.184				−0.008		0.078
$Fe^1\ d_{x^2-y^2}$	−0.184	−0.023					0.143	
$Fe^1\ d_{xy}$			0.073					0.328
$Fe^1\ d_{yz}$				−0.012				
$Fe^1\ d_{zx}$					0.012			

$t^{pp}_{\alpha\ell,\beta\ell'}$	$As^1\ p_x$	$As^1\ p_y$	$As^1\ p_z$	$As^2\ p_x$	$As^2\ p_y$	$As^2\ p_z$
$As^1\ p_x$	0.650			0.311	0.111	0.297
$As^1\ p_y$		0.027			0.311	
$As^1\ p_z$			0.048			0.389

$t^{dp}_{\alpha\ell,\beta\ell'}$	$As^1\ p_x$	$As^1\ p_y$	As^1
$Fe^1\ d_{3z^2-r^2}$	0.646		−0.2
$Fe^1\ d_{x^2-y^2}$	0.276		0.56
$Fe^1\ d_{xy}$		0.694	
$Fe^1\ d_{yz}$		0.319	
$Fe^1\ d_{zx}$	0.783		0.16

ε_ℓ	$d_{3z^2-r^2}$	$d_{x^2-y^2}$	d_{xy}	d_{yz}	d_{zx}	p_x	p_y	p_z
	−0.687	−0.610	−0.921	−0.820	−0.820	−1.789	−1.789	−2.173

Table 1: Tight-binding parameters (in units of eV) for the *d-p* Hamiltonian eq. (2). It is noted that we define the *d-p* hopping and the in-plane *p-p* hopping parameters along *x*-axis.

Due to the weak crystalline electric field from the As^{3-} ions tetrahedrally arranged around a Fe atom and the strong hybridization between the Fe 3*d* orbitals, the resulting energy bands have very complicated structure. The Fermi surface for the *d-p* tight-binding Hamiltonian is shown in Fig. 4 (b). We can see nearly circular hole Fermi surfaces (FS0, FS1 and FS2) around the Γ point and elliptical electron Fermi surfaces (FS3 and FS4) around the *M* point, where d_{yz}, d_{zx} and/or $d_{x^2-y^2}$ orbital characters are the most dominant. These results are consistent with the previous first principle calculations [42, 43, 44, 45, 46].

The Coulomb interaction part of the Hamiltonian is given as follows,

$$
\begin{aligned}
H_{\text{int}} &= \frac{1}{2}U \sum_i \sum_\ell \sum_{\sigma\neq\bar\sigma} d^\dagger_{i\ell\sigma} d^\dagger_{i\ell\bar\sigma} d_{i\ell\bar\sigma} d_{i\ell\sigma} \\
&+ \frac{1}{2}U' \sum_i \sum_{\ell\neq\bar\ell} \sum_{\sigma,\sigma'} d^\dagger_{i\ell\sigma} d^\dagger_{i\bar\ell\sigma'} d_{i\bar\ell\sigma'} d_{i\ell\sigma} \\
&+ \frac{1}{2}J \sum_i \sum_{\ell\neq\bar\ell} \sum_{\sigma,\sigma'} d^\dagger_{i\ell\sigma} d^\dagger_{i\bar\ell\sigma'} d_{i\ell\sigma'} d_{i\bar\ell\sigma} \\
&+ \frac{1}{2}J' \sum_i \sum_{\ell\neq\bar\ell} \sum_{\sigma\neq\bar\sigma} d^\dagger_{i\ell\sigma} d^\dagger_{i\ell\bar\sigma} d_{i\bar\ell\bar\sigma} d_{i\bar\ell\sigma},
\end{aligned}
\tag{3}
$$

where U and U' are the intra- and inter-orbital direct terms, respectively, and J and J' are the Hund's coupling and the pair-transfer, respectively. For the isolated atoms, the relations between Coulomb matrix elements $U = U' + 2J$ and $J = J'$ are derived due to the rotational invariance of the Coulomb interaction and the reality of the wave functions, respectively [47]. For the atoms in the crystal, however, the relation is not satisfied generally due to the crystallographic effects and the many body effects due to the Coulomb interaction which will be discussed later. Therefore, we treat U, U', J and J' as independent parameters in the present paper.

Now we consider the effect of the phonon and the electron-phonon interaction parts of the Hamiltonian H_{ph} and $H_{\text{el-ph}}$ which includes the phonon energy ω_s and the electron-phonon coupling constant $g^{\ell\ell'}_s$ between the orbital ℓ and ℓ', respectively, where s represents the phonon mode. In the present paper, we consider the B_{1g}, E_g and orthorhombic modes as shown in Figs.

where $d_{i\ell\sigma}$ is the annihilation operator for Fe-3*d* electrons with spin σ in the orbital ℓ at the site i and $p_{im\sigma}$ is the annihilation operator for As-4*p* electrons with spin σ in the orbital m at the site i. In eq. (2), the transfer integrals $t^{dd}_{i,j,\ell,\ell'}$, $t^{pp}_{i,j,m,m'}$, $t^{dp}_{i,j,\ell,m}$ and the atomic energies ε^d_ℓ, ε^p_m are determined so as to fit both the energy and the weights of orbitals for each band obtained from the tight-binding approximation to those from the density functional calculation. Similar models have been used by the other authors[39, 40, 41] but the model parameters are different from ours. The doping concentration x corresponds to the number of electrons per unit cell $n = 24 + 2x$ in the present model.

In Fig. 4 (a), we show the band structure obtained from the *d-p* tight-binding Hamiltonian eq. (2), where the tight-binding parameters are listed in Table 1 [31], together with that obtained from the density functional calculation. It is found that the former reproduces the latter very well. We note that the weights of orbitals also agree very well with each other (not shown). The result of our density functional calculation is similar to that previously reported by the other authors [42, 43, 44, 45, 46, 21].

4

2 (g), (h) and (i) [15]. We note that the orthorhombic mode is not a normal coordinate but a general coordinate which is given by a linear combination of normal coordinates including both optical and acoustic modes. To avoid the difficulty with many phonon modes, we treat the orthorhombic mode as a local phonon similar to the B_{1g} and E_g modes as a simplest first step in including the orthorhombic mode. The resulting phonon and the electron-phonon interaction parts of the Hamiltonian are given as,

$$H_{\text{ph}} = \sum_i \sum_s \omega_s b_{is}^\dagger b_{is}, \tag{4}$$

$$H_{\text{el-ph}} = \sum_i \sum_s \sum_{\ell,\ell'} \sum_\sigma g_s^{\ell\ell'} d_{i\ell\sigma}^\dagger d_{i\ell'\sigma}(b_{is}^\dagger + b_{is}), \tag{5}$$

where b_{is} is the annihilation operator for the phonon of the mode s (B_{1g}, E_g^1, E_g^2 and θ) at the site i, ω_s is the phonon frequency and $g_s^{\ell\ell'}$ is the electron-phonon coupling. We note that E_g^1 and E_g^2 correspond to the oscillation along the x- and y-axis, respectively, and θ denotes the orthorhombic mode (see Fig. 2).

Following refs. 29 and 30, we expand the electrostatic potential variance for Fe-$3d$ electrons from the four surrounding As^{4-} ions due to the oscillations of the Fe atoms for the B_{1g} and E_g modes in the displacement of the Fe atoms up to the first order and expand that in the x, y and z coordinates up to the second order. The resulting electron-phonon coupling matrix elements of the B_{1g} and E_g phonons are given as follows,

$$\sqrt{3}g_{E_g^1}^{15} = g_{E_g^1}^{25} = g_{E_g^1}^{34} = -\sqrt{3}g_{E_g^2}^{14} = g_{E_g^2}^{24} = -g_{E_g^2}^{35} = g_{E_g}, \tag{6}$$

$$g_{B_{1g}}^{44} = -g_{B_{1g}}^{55} = \sqrt{3}/2 g_{B_{1g}}^{12} = g_{B_{1g}}, \tag{7}$$

$$g_s^{\ell\ell'} = g_s^{\ell'\ell}, \tag{8}$$

$$g_s^{\ell\ell'} = 0 \quad \text{(otherwise)}. \tag{9}$$

In addition, we also consider the electron-phonon coupling matrix elements of the orthorhombic phonon g_θ^{45} coupled with the transverse d_{yz}-d_{zx} (i. e., the longitudinal $d_{y'z}$-$d_{zx'}$) orbital fluctuation and g_θ^{13} coupled with the transverse $d_{3z^2-r^2}$-d_{xy} orbital fluctuation [15].

Within the RPA [48, 49, 50], the spin susceptibility $\hat{\chi}^s(q)$ and the charge-orbital susceptibility $\hat{\chi}^c(q)$ are given in the 50×50 matrix representation as follows [15, 24, 31, 33],

$$\hat{\chi}^s(q) = [\hat{I} - \hat{\chi}^{(0)}(q)\hat{S}]^{-1}\hat{\chi}^{(0)}(q), \tag{10}$$

$$\hat{\chi}^c(q) = [\hat{I} + \hat{\chi}^{(0)}(q)\hat{C}]^{-1}\hat{\chi}^{(0)}(q) \tag{11}$$

with the noninteracting susceptibility

$$\chi_{\ell_1\ell_2,\ell_3\ell_4}^{(0)\,\alpha,\beta}(q) = -\frac{T}{N}\sum_k G_{\ell_3\ell_1}^{\beta\alpha}(k)G_{\ell_2\ell_4}^{\alpha\beta}(k+q), \tag{12}$$

where α, β ($=A, B$) represent two Fe sites, ℓ represents Fe $3d$ orbitals, $\hat{G}(k) = [(i\varepsilon_n + \mu)\hat{I} - \hat{H}_0(\boldsymbol{k})]^{-1}$ is the noninteracting Fe-$3d$ electron Green's function in the 10×10 matrix representation with the chemical potential μ, $\hat{H}_0(\boldsymbol{k})$ is the kinetic part of the Hamiltonian with the momentum $\boldsymbol{k}$ in eq. (2), $k = (\boldsymbol{k}, i\varepsilon_n)$, $q = (\boldsymbol{q}, iv_m)$ and $\varepsilon_n = (2n+1)\pi T$ and $v_m = 2m\pi T$ are the fermionic and bosonic Matsubara frequencies, respectively. In

eqs. (10) and (11), the bare vertices for the spin and charge-orbital susceptibilities $\hat{S}$ and $\hat{C}$ are given by [32]

$$(\hat{S})_{\ell_1\ell_2,\ell_3\ell_4}^{\alpha,\beta} = (\hat{U}^s)_{\ell_1\ell_2,\ell_3\ell_4}^{\alpha,\beta}, \tag{13}$$

$$(\hat{C})_{\ell_1\ell_2,\ell_3\ell_4}^{\alpha,\beta} = (\hat{U}^c)_{\ell_1\ell_2,\ell_3\ell_4}^{\alpha,\beta} - 2\delta_{\alpha\beta}\sum_s g_s^{\ell_2\ell_1}g_s^{\ell_3\ell_4}D_s(iv_m), \tag{14}$$

where the $D_s(iv_m) = 2\omega_s/(v_m^2 + \omega_s^2)$ is the local phonon Green's function for the mode s and $\hat{U}^s$ and $\hat{U}^c$ are the bare vertices due to the Coulomb interaction given as follows,

$$\hat{U}^s(\hat{U}^c) = \begin{cases} U\ (U) & (\alpha = \beta,\ \ell_1 = \ell_2 = \ell_3 = \ell_4) \\ U'\ (-U'+2J) & (\alpha = \beta,\ \ell_1 = \ell_3 \neq \ell_2 = \ell_4) \\ J\ (2U'-J) & (\alpha = \beta,\ \ell_1 = \ell_2 \neq \ell_3 = \ell_4) \\ J'\ (J') & (\alpha = \beta,\ \ell_1 = \ell_4 \neq \ell_2 = \ell_3) \\ 0 & \text{(otherwise)}. \end{cases} \tag{15}$$

It is noted that when the largest eigenvalue λ_{spin} ($\lambda_{\text{c-o}}$) of $\hat{\chi}^{(0)}(q)\hat{S}$ ($-\hat{\chi}^{(0)}(q)\hat{C}$) reaches unity, the magnetic (charge-orbital) instability occurs.

The linearized Eliashberg equation is given by

$$\lambda_{\text{sc}}\Delta_{\ell\ell'}^{\alpha\beta}(k) = -\frac{T}{N}\sum_{k'}\sum_{\ell_1\ell_2\ell_3\ell_4}\sum_{\alpha'\beta'} V_{\ell\ell_1,\ell_2\ell'}^{\alpha,\beta}(k - k')$$
$$\times\ G_{\ell_3\ell_1}^{\alpha'\alpha}(-k')\Delta_{\ell_3\ell_4}^{\alpha'\beta'}(k')G_{\ell_4\ell_2}^{\beta'\beta}(k'), \tag{16}$$

where $\Delta_{\ell\ell'}^{\alpha\beta}(k)$ is the gap function and $V_{\ell_1\ell_2,\ell_3\ell_4}^{\alpha,\beta}(q)$ is the effective pairing interaction for the spin-singlet state. Within the RPA [48, 49, 50], $V_{\ell_1\ell_2,\ell_3\ell_4}^{\alpha,\beta}(q)$ is given in the 50×50 matrix,

$$\hat{V}(q) = \eta\hat{S}\hat{\chi}^s(q)\hat{S} - \frac{1}{2}\hat{C}\hat{\chi}^c(q)\hat{C} + \frac{1}{2}(\hat{S} + \hat{C}), \tag{17}$$

where $\eta = \frac{3}{2}$ for the spin-singlet state and $\eta = -\frac{1}{2}$ for the spin-triplet state. The linearized Eliashberg equation (16) is solved to obtain the gap function $\Delta_{\ell\ell'}^{\alpha\beta}(k)$ with the eigenvalue λ_{sc}. At $T = T_c$, the largest eigenvalue λ_{sc} becomes unity.

3. Calculated results

In this section, we present the RPA results for the electronic states and the superconductivity based on the recent published work [15] by using a different parameter set of the electron-phonon coupling matrix elements. In addition, we show the Hartree-Fock phase diagram including the structural and the magnetic phase transitions [51] which was discussed but not explicitly shown in the previous paper [15]. We also present a more detailed analysis on the ultrasonic softening of the elastic constants [13, 14] on the basis of the RPA and the self-consistent renormalization (SCR) theory [52].

In the numerical calculations for eqs. (10)-(17), we use 32×32 $\boldsymbol{k}$ point meshes and 512 Matsubara frequencies ($-511\pi T \leq \varepsilon_n \leq 511\pi T$). For simplicity, we set $\omega_{B_{1g}} = \omega_{E_g^1} = \omega_{E_g^2} = \omega_\theta = \omega_0 = 0.02$eV as done in the previous study [15, 33]. To reproduce the experimental results that the elastic softening is observed exclusively for the C_{66} mode [14], we assume $g_{B_{1g}} = g_{E_g} = \frac{g_\theta^{45}}{2}$ and $g_\theta^{13} = 0$, and put $g_\theta^{45} = g$ [53]. Here and hereafter, we measure the energy in units of eV.
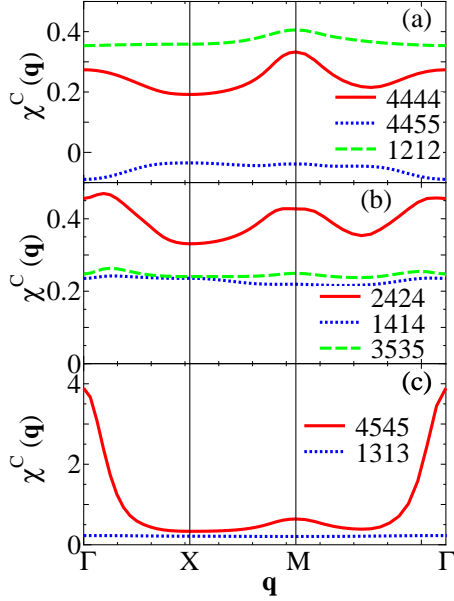
Figure 5: (Color online) Several components of the charge-orbital susceptibility $\hat{\chi}^c(\boldsymbol{q}, \omega = 0)$ for $U' = 0.6$, $J = J' = 0.2$, $U = U' + 2J = 1.0$ and $g = 0.089$ at $x = 0.1$ and $T = 0.035$, where we number the Fe-3d orbitals as follows: $d_{3z^2-r^2}(1)$, $d_{x^2-y^2}(2)$, $d_{xy}(3)$, $d_{yz}(4)$, $d_{zx}(5)$.

Fig. 5 shows several components of the static charge-orbital susceptibility $\hat{\chi}^c(\boldsymbol{q}, 0)$ for $U' = 0.6$, $J = 0.2$ and $g = 0.089$ at $x = 0.1$ and $T = 0.035$. In this case, the dimensionless electron-phonon coupling parameter is given by $\lambda = 2g^2\rho_0/\omega_0 \sim 2g^2/\omega_0 = 0.80$ with the density of states at the Fermi level $\rho_0 \sim 1/\text{eV}$. We find that, when T decreases, the transverse d_{yz}-d_{zx} orbital susceptibility $[\hat{\chi}^c(\boldsymbol{q}, 0)]^{A,A}_{45,45}$ with $\boldsymbol{q} \sim (0, 0)$, which is equivalent to the longitudinal $d_{y'z}$-$d_{zx'}$ one, is most enhanced as compared to the other orbital and magnetic susceptibilities (not shown) due to the cooperative effects of the electron-phonon interaction with the orthorhombic mode and the inter-orbital Coulomb interaction U' [31, 33]. We note that, the incommensurate peaks around $\boldsymbol{q} = (0, 0)$ were observed in the previous work [15] where the different parameter set of the electron-phonon coupling matrix elements was used. However, the resulting pairing state and the phase diagram are essentially unchanged as shown below.

In Figs. 6 (a)-(d), we show several components of the superconducting gap function with the lowest Matsubara frequency $\hat{\Delta}(\boldsymbol{k}, i\pi T)$ obtained by solving the linearized Eliashberg equation (16) for the same parameters as in Fig. 5. In this case, the enhanced orbital susceptibility $\hat{\chi}^c(q)$ for $\boldsymbol{q} \sim (0, 0)$ (see Fig. 5), i. e., the ferro-orbital fluctuation yields the large negative value of the effective pairing interactions $\hat{V}(q)$ for $\boldsymbol{q} \sim (0, 0)$ due to the 2nd term of r.h.s. in eq. (17), resulting in the gap function without sign change, i. e., the s_{++}-wave state. For comparison, we also show the gap function in the case with a smaller (larger) value of g (U'), $U' = 1.48$, $J = 0.2$ and $g = 0.032$, in Figs. 6 (e)-(h). In this case, the enhanced magnetic susceptibility $\hat{\chi}^s(q)$ for $\boldsymbol{q} \sim (\pi, \pi)$ (not shown), i. e., the stripe-type AFM fluctuation yields the large positive value of $\hat{V}(q)$ for $\boldsymbol{q} \sim (\pi, \pi)$ due to
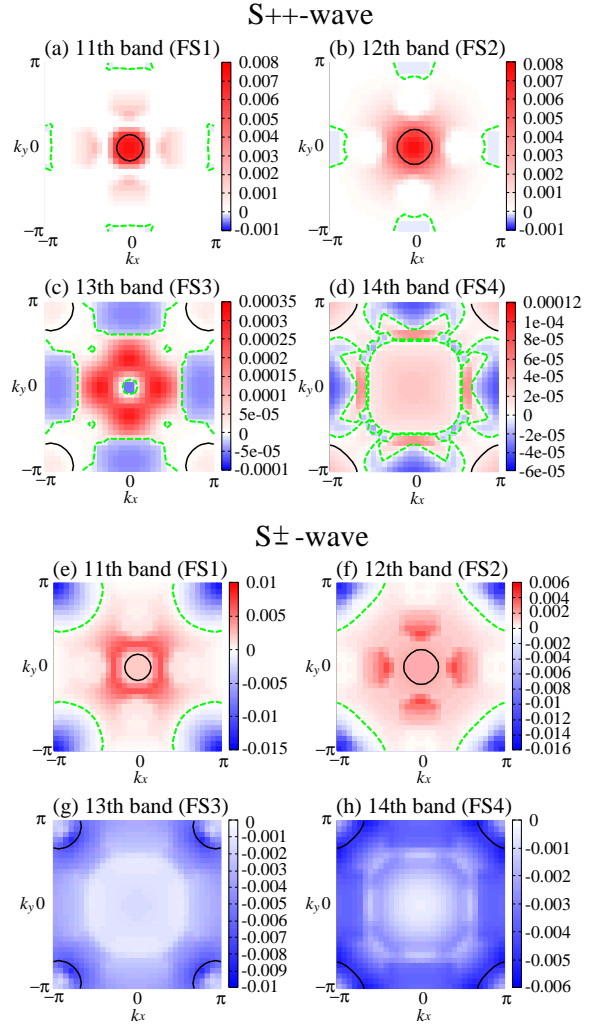

Figure 6: (Color online) Several components of the gap function $\hat{\Delta}(\boldsymbol{k}, i\pi T)$ for $U' = 0.6$, $J = 0.2$ and $g = 0.089$ at $x = 0.1$ and $T = 0.035$ (a)-(d), and those for $U' = 1.48$, $J = 0.2$ and $g = 0.032$ at $x = 0.1$ and $T = 0.034$ (e)-(h).

the 1st term of r.h.s. in eq. (17), resulting in the gap function with sign change, i. e., the $s_{\pm}$-wave state. We note that, the effects of the ferro-orbital and the AFM fluctuations on the superconductivity do not compete to each other as they are mainly responsible for the different $\boldsymbol{q}$ regions in $\hat{V}(q)$, in contrast to the case with the antiferro-orbital and the AFM fluctuations.

Fig. 7 (a) shows the phase diagram on the x-T plane in the case with a large g, $U' = 0.6$, $J = 0.2$ and $g = 0.065$. As the numerical calculation to obtain the phase diagram consumes much CPU time, we show the same results as in the previous work [15] where the different parameter set of the electron-phonon coupling matrix elements was used [53]. When T decreases, the ferro-orbital susceptibility $[\hat{\chi}^c(\boldsymbol{0}, 0)]^{A,A}_{45,45}$ (see Fig. 5 (c)) diverge at a critical temperature T_Q. Below T_Q, the ferro-orbital order with different occupations of the $d_{y'z}$ and $d_{zx'}$ orbitals occurs and induces the orthorhombic distortion resulting in the tetragonal-orthorhombic structural transition at $T_s = T_Q$. When approaching T_Q, the ferro-orbital fluctuation is largely enhanced and me-
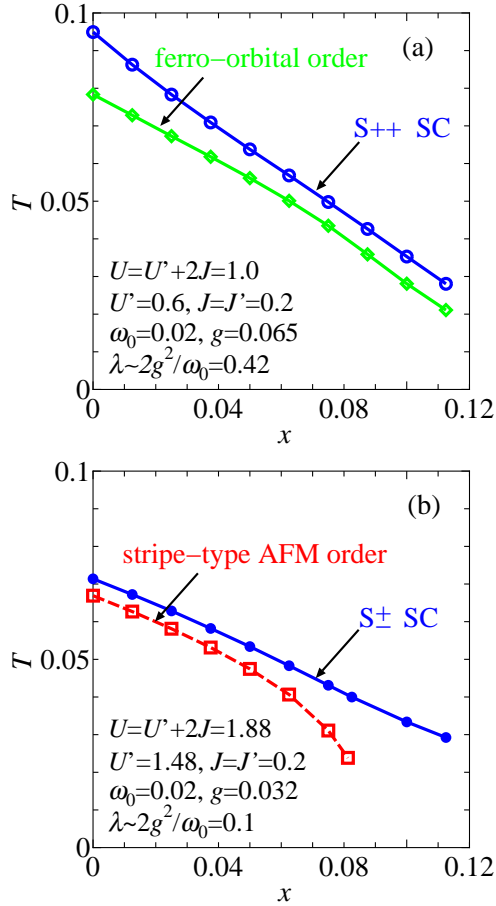
Figure 7: (Color online) RPA phase diagram on the x-T plane for $U' = 0.6$, $J = J' = 0.2$, $U = U' + 2J = 1.0$ and $g = 0.065$ (a) and that for $U' = 1.48$, $J = J' = 0.2$, $U = U' + 2J = 1.88$ and $g = 0.032$ (b). The symbols represent the instabilities for the ferro-orbital order (diamonds), the stripe-type AFM order (squares), the s_{++}-wave superconductivity (open circles) and the $s_{\pm}$-wave superconductivity (closed circles), respectively (reproduced from Ref. [15]).
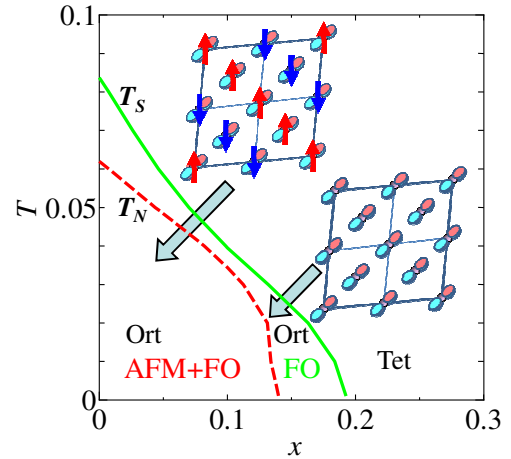

Figure 8: (Color online) Hartree-Fock phase diagram of the 16-band d-p model for iron pnictides in the presence of both the Coulomb interaction between Fe d-electrons and the electron-lattice coupling g with the orthorhombic mode in the case with a large g, where the explicit values of the parameters in the model is shown in Ref. [51]. $T_s(= T_Q)$ is the second order phase transition temperature of the tetragonal-orthorhombic structural transition accompanied by the $d_{y'z} - d_{zx'}$ ferro-orbital transition and T_N is that of the stripe-type AFM transition, respectively.

diates the s_{++}-wave superconductivity (see Figs. 6 (a)-(d)).

We also investigate the same model within the Hartree-Fock approximation for the Coulomb interaction between Fe d-electrons together with the adiabatic approximation for the electron-lattice coupling g with the orthorhombic mode [51]. For a large g case, we obtain the phase diagram shown in Fig. 8, where $T_s(= T_Q)$ is the second order phase transition temperature from the tetragonal phase ($T > T_s$) to the orthorhombic phase ($T < T_s$) with the $d_{y'z} - d_{zx'}$ ferro-orbital order and T_N is that of the stripe-type AFM transition. The obtained ordered pattern below T_N is consistent with the experimental observation where the Fe spins are aligned antiferromagnetically along the longer axis while those are aligned ferromagnetically along the shorter axis [10] (see Fig. 8). We note that the obtained phase diagram shown in Fig. 8 is consistent with 1111 system such as RFeAsO$_{1-x}$F$_x$ where $T_s = T_Q$ is always higher than T_N, while, for a relatively-small g case, we also obtain the phase diagram (not shown) consistent with 122 system such as Ba(Fe$_{1-x}$Co$_x$)$_2$As$_2$ where the simultaneous first-order phase

transition $T_s = T_Q = T_N$ for $x = 0$ splits into two transitions $T_s = T_Q > T_N$ with doping x. In both cases, the longitudinal $d_{y'z} - d_{zx'}$ ferro-orbital fluctuation, which is responsible for the softening of C_{66}, dominates over the AFM fluctuation above $T_s = T_Q$ where the s_{++}-wave pairing without sign reversal of the superconducting gap function is mediated by the ferro-orbital fluctuation as shown in Fig. 7 (a).

For comparison, we also show the x-T phase diagram in the case with a smaller (larger) value of g (U'), $U' = 1.48$, $J = 0.2$ and $g = 0.032$, in Fig. 7 (b). When T decreases, the magnetic susceptibility with $q \sim (\pi, \pi)$ diverges at T_N below which the stripe-type AFM order occurs and induces the ferro-orbital order [18] together with the orthorhombic distortion resulting in the tetragonal-orthorhombic structural transition at $T_s = T_N$, although the RPA result of T_Q is smaller than that of T_N. When approaching T_N, the AFM fluctuation is largely enhanced and mediates the $s_{\pm}$-wave superconductivity [20, 21, 24]. In this case, the simultaneous phase transition takes place at $T_s = T_N$ even for $x > 0$ and is inconsistent with the phase diagram of doped iron pnictides with $T_s > T_N$ which is reproduced for a large g case mentioned above.

Here, we discuss the softening of the elastic constant C_{66} observed in the recent ultrasonic experiments [11, 12, 13, 14]. As mentioned before, the elastic constant C_Γ includes the contribution proportional to the O_Γ quadrupole susceptibility. Then, we calculate the uniform quadrupole susceptibilities for O_{xy}, $O_{yz/zx}$ and $O_{x^2-y^2}$, $\chi_{O_{xy}}$, $\chi_{O_{yz/zx}}$ and $\chi_{O_{x^2-y^2}}$ [54], which are given by linear combinations of the various components of the charge-orbital susceptibility $\hat{\chi}^c$ with $q = (0, 0)$ and $\omega = 0$ (see Fig. 5). In Fig. 9, the quadrupole susceptibilities obtained from the RPA are plotted as functions of the temperature for the same parameters as in Fig. 5. We find that $\chi_{O_{xy}}$ is largely enhanced due to
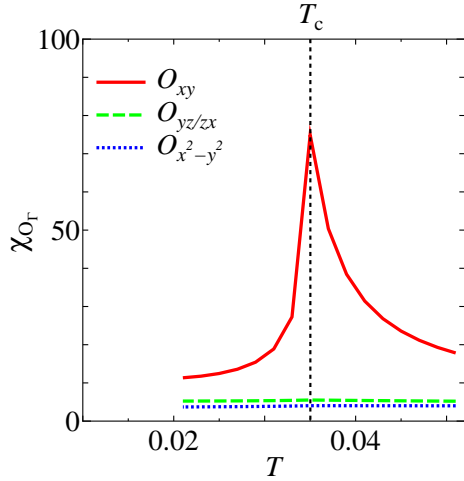
Figure 9: (Color online) Temperature dependence of the quadrupole susceptibilities $\chi_{O_{xy}}$, $\chi_{O_{yz/zx}}$ and $\chi_{O_{x^2-y^2}}$ with $q = (0,0)$ and $\omega = 0$ for $U' = 0.6$, $J = J' = 0.2$, $U = U' + 2J = 1.0$ and $g = 0.089$ at $x = 0.1$.
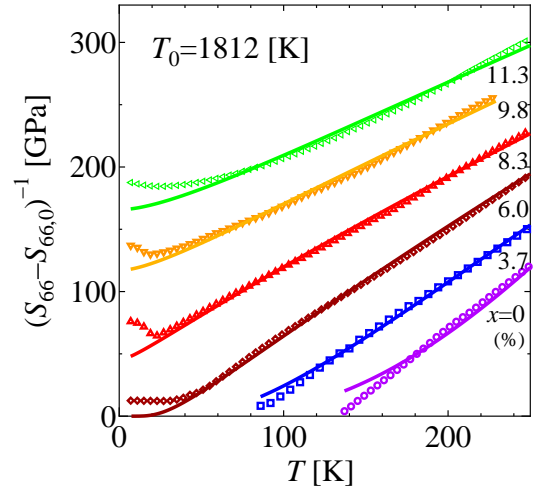

Figure 10: Temperature dependence of $(S_{66} - S_{66,0})^{-1}$ in Ba(Fe$_{1-x}$Co$_x$)$_2$As$_2$. The marks represent the experimental results by Yoshizawa *et al.* [13] and the solid lines represent the fitting results from the SCR theory (see in the text).

the enhancement of $[\hat{\chi}^c(0,0)]_{45,45}^{A,A}$ as shown in Fig. 5 (c). When T decreases, $\chi_{O_{xy}}$ increases for $T > T_c$ and shows divergent behavior towards $T_Q(< T_c)$ where $[\hat{\chi}^c(0,0)]_{45,45}^{A,A}$ diverges (see Fig. 7 (a)), while it decreases for $T < T_c$ due to the effect of the superconducting gap. This T dependence well accounts for the experimental observation where C_{66} decreases with decreasing T (softening) for $T > T_c$ while increases for $T < T_c$ [13, 14]. In contrast to $\chi_{O_{xy}}$, $\chi_{O_{yz/zx}}$ and $\chi_{O_{x^2-y^2}}$ are almost independent of T. This is also consistent with the ultrasonic experiments where no softening is observed in $C_E = (C_{11} - C_{12})/2$ and C_{44} [14] which include the contributions in proportion to $\chi_{O_{yz/zx}}$ and $\chi_{O_{x^2-y^2}}$, respectively.

The detailed analysis of the elastic constant C_{66} for Ba(Fe$_{1-x}$Co$_x$)$_2$As$_2$ [13] has revealed that the uniform O_{xy} quadrupole susceptibility shows the Curie-Weiss like behavior in a wide temperature range from the room temperature down to the structural or the superconducting transition temperature, where the Weiss temperature monotonically decreases with increasing the Co doping x and is positive for $x \lesssim 0.07$ while negative for $x \gtrsim 0.07$. To analyze such behavior, we employ the SCR theory originally developed for itinerant electron magnetism [52] and recently extended for orbital fluctuations [55]. The SCR theory includes the mode coupling effects neglected in the RPA and enables us to describe the the Curie-Weiss like behavior of the magnetic (orbital) susceptibility in a wide temperature range in contrast to the RPA [52]. The present analysis is a straight forward extension of the standard SCR theory to the quadrupole fluctuations in itinerant electron systems such as doped iron pnictides. The brief formulation is given in Appendix A.

To obtain the T dependence of the uniform O_{xy} quadrupole susceptibility $\chi_{O_{xy}}$, we need to solve the SCR equation given in eq. (A.6) with $Q = 0$, $\theta = 1$ and $D = 2$ which includes three parameters, y_0, y_1 and T_0, corresponding to the inverse of the

quadrupole susceptibility at $T = 0$, the mode coupling constant and the energy scale of the quadrupole fluctuation, respectively (see Appendix A). We assume that $T_0 = 1812$K [56] is independent of the Co doping x while y_0 and y_1 depend on x and are determined so as to fit the T dependence of $\chi_{O_{xy}}$ from the SCR to that from the ultrasonic experiments as possible. Fig. 10 shows the fitting results of the T dependence of $(S_{66} - S_{66,0})^{-1}$ which is proportional to $1/\chi_{O_{xy}}$ obtained from the SCR theory together with the experimental results by Yoshizawa *et al.* [13], where $S_{66} = C_{66}^{-1}$ is the elastic compliance and $S_{66,0}$ is the back ground part of that. It is found that the overall behavior of the experiments is well reproduced by the SCR theory for the whole temperature and doping range. Especially, for $x = 0.06$, 0.083 and 0.098, the SCR results are in good agreement with the experimental results at $T > T_c$ or $T > T_s$. On the other hand, for $x = 0$ and 0.037, the deviation between the SCR and experimental results becomes significant at low temperature. This is considered due to the effect of the three dimensionality which is neglected in the present SCR theory with $D = 2$ where no long-range order takes place at finite temperature in contrast to the case with $D = 3$. It is expected that the fitting results for $x = 0$ and 0.037 are improved at low temperature by using the SCR theory with $D = 3$.

Fig. 11 shows the doping dependence of y_0 obtained by fitting the experimental results in Ba(Fe$_{1-x}$Co$_x$)$_2$As$_2$ (see Fig. 10). It is found that y_0 monotonically increases with increasing x and crosses 0 at $x \sim 0.073$ where $\chi_{O_{xy}}$ diverges at $T = 0$ (see (A.6)). This means that the O_{xy} ferro-quadrupole (or the $d_{y'z}$-$d_{zx'}$ ferro-orbital) quantum critical point (QCP) is located at $x = x_{\text{QCP}} \sim 0.073$. Remarkably, the superconducting transition temperature T_c shows a maximum at $x \sim x_{\text{QCP}}$ [9, 57], where the orbital fluctuation is expected to dominate over the AFM fluctuation and mediate the s_{++}-wave superconductivity [58].
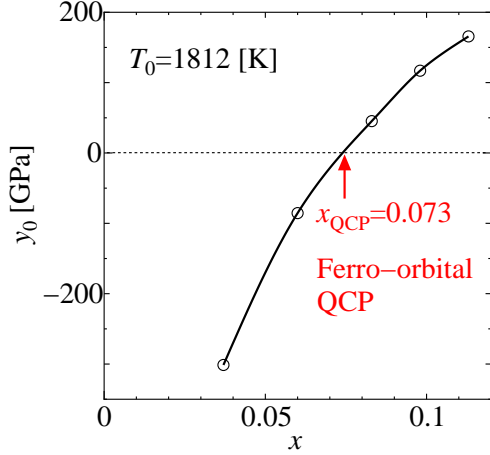
8

Figure 11: Doping dependence of y_0 in the SCR theory obtained by fitting the experimental results in Ba(Fe$_{1-x}$Co$_x$)$_2$As$_2$ (see in the text).

4. Sumary and discussions

In summary, we have shown that the ferro-orbital fluctuation relevant to the ultrasonic softening of C_{66} is enhanced by the electron-phonon coupling g with the orthorhombic mode and diverges at T_Q below which the ferro-orbital order with different occupations of the $d_{y'z}$ and $d_{zx'}$ orbitals occurs and induces the orthorhombic distortion resulting in the tetragonal-orthorhombic structural transition at $T_s = T_Q$. Near the transition, the s_{++}-wave superconductivity is realized due to the ferro-orbital fluctuation. The obtained x-T phase diagram is consistent with the phase diagram of doped iron pnictides with $T_s > T_N$, in contrast to a relatively small g case with $T_s = T_N$ where the $s_{\pm}$-wave superconductivity is realized due to the antiferromagnetic fluctuation.

We have also analyzed the experimental results of C_{66} in Ba(Fe$_{1-x}$Co$_x$)$_2$As$_2$, where the Curie-Weiss like behavior in a wide temperature range is observed, based on the phenomenological SCR theory which includes mode coupling effects neglected in the RPA. It has been found that the experimental results are well reproduced by the SCR theory for quadrupole fluctuations and there exists the O_{xy} ferro-quadrupole ($d_{y'z}$-$d_{zx'}$ ferro-orbital) QCP at $x = x_{QCP} \sim 0.073$, around which the ferro-orbital fluctuation is largely enhanced at low temperature and the superconducting transition temperature T_c is expected to show a maximum as observed in the experiments.

For both cases with s_{++}- and $s_{\pm}$-wave superconductivities, the RPA result of T_c is always higher than that of $T_s(= T_Q)$ and/or T_N, where the orbital and/or the magnetic fluctuations diverge. In experiments, however, for small doping x, $T_s(= T_Q)$ and/or T_N are higher than T_c. With including the effects of the self-energy correction and the vertex correction neglected in the RPA, it is expected that the ferro-orbital order and/or the antiferromagnetic orders are realized for relatively small x, while the superconductivity is realized for relatively large x and shows a maximum around the QCP mentioned above. The explicit calculations to include such effects by using the dynamical mean-field theory [59] and the self-consistent fluctuation theory [60] are now under the way.

The obtained s_{++}-wave superconductivity seems to be consistent with experimental results of iron pnictides including the impurity effects. The enhanced ferro-orbital fluctuation above T_Q might be observed by experiments with a kind of external field inducing the anisotropy of x', y' axes, similar to the case with the ferromagnetic fluctuation above the Curie temperature observed by experiments with the external magnetic field. In fact, a resistivity anisotropy for $T > T_s$ is induced by uniaxial stress [61]. In the present paper, we treated the orthorhombic mode as a optical phonon, as a simplest first step. More realistic model including acoustic phonons will be discussed elsewhere.

Acknowledgement

Appendix A. SCR theory for quadrupole fluctuations

In this appendix, we briefly summrize the SCR theory for quadrupole fluctuations as a straight forward extension of the standard SCR theory for itinerant electron magnetism [52]. In the vicinity of the phase transition for the O_{xy} quadrupole order with the wave vector $\boldsymbol{Q}$, we expand the free energy F with respect to the O_{xy} quadrupole operator with the wave vector $\boldsymbol{q}$, $O_{xy}(\boldsymbol{q})$, as

$$\exp(-F/T) = \int \prod_{\boldsymbol{q}} dO_{xy}(\boldsymbol{q}) \exp(-\Psi/T) \quad (\text{A.1})$$

with

$$\begin{aligned} \Psi &= \sum_{\boldsymbol{q}} \left(\frac{1}{2\chi_{O_{xy}}^{(0)}(\boldsymbol{q})} - I \right) |O_{xy}(\boldsymbol{q})|^2 \\ &+ \frac{1}{4} F_Q \sum_{\boldsymbol{q},\boldsymbol{q}',\boldsymbol{q}''} O_{xy}(\boldsymbol{q}) O_{xy}(-\boldsymbol{q}') O_{xy}(\boldsymbol{q}'') O_{xy}(\boldsymbol{q}' - \boldsymbol{q}'') \quad (\text{A.2}) \end{aligned}$$

where I and F_Q are the phenomenological O_{xy} quadrupole-quadrupole interaction and the mode coupling constant, respectively. By performing functional derivatives in eq. (A.1) with respect to $O_{xy}(\boldsymbol{q})$ and $O_{xy}(-\boldsymbol{q})$, we obtain the following equation

$$\frac{1}{\chi_{O_{xy}}^{(0)}(\boldsymbol{Q})} - 2I + 3F_Q \langle (O_{xy}^{\text{loc}})^2 \rangle + F_Q \langle O_{xy}(\boldsymbol{Q}) \rangle^2 = \frac{1}{\chi_{O_{xy}}(\boldsymbol{Q})} \quad (\text{A.3})$$

where $O_{xy}^{\text{loc}} = \frac{1}{N} \sum_{\boldsymbol{q}} O_{xy}(\boldsymbol{q})$ is the local O_{xy} quadrupole operator and $\chi_{O_{xy}}^{(0)}(\boldsymbol{q})$ and $\chi_{O_{xy}}(\boldsymbol{q})$ are the noninteracting and interacting O_{xy} quadrupole susceptibilities. Here, we assume that the

dynamical O_{xy} quadrupole susceptibility $\chi_{O_{xy}}(\boldsymbol{Q}+\boldsymbol{q},\omega)$ can be expanded as follows,

$$\frac{1}{\chi_{O_{xy}}(\boldsymbol{Q}+\boldsymbol{q},\omega)} = \frac{1}{\chi_{O_{xy}}(\boldsymbol{Q})} + Aq^2 - iC\frac{\omega}{q^\theta}, \qquad (A.4)$$

where $\theta = 1$ for $\boldsymbol{Q} = \boldsymbol{0}$ and $\theta = 0$ for otherwise. By using the fluctuation-dissipation theorem, eq. (A.4) yields

$$\langle(O_{xy}^{loc})^2\rangle = \frac{1}{N}\sum_q \int_0^\infty \frac{d\omega}{2\pi}\coth\frac{\omega}{2T}\mathrm{Im}\chi_{O_{xy}}(\boldsymbol{Q}+\boldsymbol{q},\omega)\!(A.5)$$

Substitute eq. (A.5) into eq. (A.3), we obtain the following SCR equation

$$\frac{1}{2T_A\chi_{O_{xy}}(\boldsymbol{Q})} = y_0 + \frac{D}{2}y_1\int_0^{x_c}dx\,x^{D+\theta-1}\left[\ln u - \frac{1}{2u} - \psi(u)\right]\!(A.6)$$

with

$$y_0 = \frac{1}{2T_A\chi_{O_{xy}}(\boldsymbol{Q},T=0)}, \quad y_1 = \frac{3F_Q T_0}{T_A^2},$$

$$T_A = \frac{Aq_B^2}{2}, \quad T_0 = \frac{q_B^{2+\theta}}{2\pi}\frac{A}{C},$$

$$u = \frac{x^\theta(y+x^2)}{T/T_0}, \quad q_B = \left(\frac{2D\pi^{D-1}}{v_0}\right)^{1/D},$$

where ψ, x_c, D and v_0 represent the digamma function, the wave number cut-off, the spatial dimention and the unit cell volume, respectively. Note that we negelect the zero-point fluctuations in deriving eq. (A.6). In eq. (A.6), there are three independent parameters, y_0, y_1 and T_0, which are proportional to the inverse of the quadrupole susceptibility at $T = 0$, the mode coupling constant and the energy scale of the quadrupole fluctuation, respectively. By solving the SCR equation eq. (A.6) for a given parameter set of y_0, y_1 and T_0, we obtain the T dependence of the quadrupole susceptibility $\chi_{O_{xy}}(\boldsymbol{Q})$.

References

[1] Y. Kamihara, H. Hiramatsu, M. Hirano, H. Y. R. Kawamura, T. Kamiya, H. Hosono, J. Am. Chem. Soc. 128 (2006) 10012.
[2] Y. Kamihara, T. Watanabe, M. Hirano, H. Hosono, J. Am. Chem. Soc. 130 (2008) 3296.
[3] Z. A. Ren, W. Lu, J. Yang, W. Yi, X. L. Shen, G. C. C. Z. C. Li, X. L. Dong, L. L. Sun, F. Zhou, Z. X. Zhao, Chin. Phys. Lett. 25 (2008) 2215.
[4] C. de la Cruz, Q. Huang, J. W. Lynn, J. Li, W. R. II, J. L. Zarestky, H. A. Mook, G. F. Chen, J. L. Luo, N. L. Wang, P. Dai, Nature 453 (2008) 899.
[5] A much larger value of the ordered moment $\sim 0.65\mu_B$ is observed in the recent neutron experiment in LaFeAsO: N. Qureshi, Y. Drees, J. Werner, S. Wurmehl, C. Hess, R. Klingeler, B. Buchner, M. T. Fernandez-Diaz and M. Braden, Phys. Rev. B 82 (2010) 184521.
[6] J. Zhao, Q. Huang, C. de la Cruz, S. Li, J. W. Lynn, Y. Chen, M. A. Green, G. F. Chen, G. Li, Z. Li, J. L. Luo, N. L. Wang, P. Dai, Nature Materials 7 (2008) 953.
[7] H. Luetkens, H.-H. Klauss, M. Kraken, F. J. Litterst, T. Dellmann, C. H. R. Klingeler, R. Khasanov, A. Amato, C. Baines, M. Kosmala, O. Schumann, M. Braden, J. Hamann-Borrero, N. Leps, A. Kondrat, G. Behr, J. Werner, B. Büchne, Nature Materials 8 (2009) 305.
[8] D. R. Parker, M. J. P. Smith, T. Lancaster, A. J. Steele, I. Franke, P. J. Baker, F. L. Pratt, M. J. Pitcher, S. J. Blundell, S. J. Clarke, Phys. Rev. Lett. 104 (2011) 057007.
[9] S. Nandi, M. G. Kim, A. Kreyssig, R. M. Fernandes, D. K. Pratt, A. Thaler, N. Ni, S. L. Bud'ko, P. C. Canfield, J. Schmalian, R. J. McQueene, A. I. Goldman, Phys. Rev. Lett. 104 (2010) 057006.
[10] T.-W. Huang, T.-K. Chen, K.-W. Y.eh, C.-T. Ke, C. L. Chen, Y.-L. Huang, F.-C. Hsu, M.-K. Wu, P. M. Wu, M. Avdeev, A. J. Studer, Phys. Rev. B 82 (2010) 104502.
[11] M. A. McGuire, A. D. Christianson, A. S. Sefat, B. C. Sales, M. D. Lumsden, R. Jin, E. A. Payzant, D. Mandrus, Y. Luan, V. Keppens, V. Varadarajan, J. W. Brill, R. P. Hermann, M. T. Sougrati, F. Grandjean, G. J. Long, Phys. Rev. B 78 (2008) 094517.
[12] R. M. Fernandes, L. H. VanBebber, S. Bhattacharya, P. Chandra, V. Keppens, D. Mandrus, M. A. McGuire, B. C. Sales, A. S. Sefat, J. Schmalian, Phys. Rev. Lett. 105 (2010) 157003.
[13] M. Yoshizawa, D. Kimura, T. Chiba, A. Ismayil, Y. Nakanishi, K. Kihou, C. H. Lee, A. Iyo, H. Eisaki, M. Nakajima, S. Uchida, arXiv:1111.0366, to be published in J. Phys. Soc. Jpn. .
[14] T. Goto, R. Kurihara, K. Araki, K. Mitsumoto, M. Akatsu, Y. Nemoto, S. Tatematsu, M. Sato, J. Phys. Soc. Jpn. 80 (2011) 073702.
[15] Y. Yanagi, Y. Yamakawa, N. Adachi, Y. Ōno, J. Phys. Soc. Jpn. 79 (2010) 123707.
[16] T. Goto, private communication.
[17] T. Yildirim, Phys. Rev. Lett 101 (2008) 057010.
[18] K. Kubo, P. Thalmeier, J. Phys. Soc. Jpn. 78 (2009) 2009.
[19] E. Bascones, M. J. Calderon, B. Valenzuela, Phys. Rev. Lett. 104 (2010) 227201.
[20] I. I. Mazin, D. J. Singh, M. D. Johannes, M. H. Du, Phys. Rev. Lett. 101 (2008) 057003.
[21] K. Kuroki, S. Onari, R. Arita, H. Usui, Y. Tanaka, H. Kontani, H. Aoki, Phys. Rev. Lett. 101 (2008) 087004.
[22] H. Ikeda, J. Phys. Soc. Jpn. 77 (2008) 123707.
[23] T. Nomura, J. Phys. Soc. Jpn. 78 (2009) 0347160.
[24] Y. Yanagi, Y. Yamakawa, Y. Ōno, J. Phys. Soc. Jpn. 77 (2008) 123701.
[25] D. C. Johnston, Adv. Phys. 59 (2010) 803.
[26] A. Kawabata, S. C. Lee, T. Moyoshi, Y. Kobayashi, M. Sato, J. Phys. Soc. Jpn. 77 (2008) 103704.
[27] M. Sato, Y. Kobayashi, S. Lee, H.Takahashi, E. Satomi, Y. Miura, J. Phys. Soc. Jpn. 79 (2010) 014710.
[28] S. Onari, H. Kontani, Phys. Rev. Lett. 103 (2009) 177001.
[29] K. Sano, Y. Ōno, J. Phys. Soc. Jpn. 78 (2009) 124706.
[30] M. Okumura, N. Nakai, H. Nakamura, N. Hayashi, S. Yamada, M. Machida, Physica C 469 (2009) 932.
[31] Y. Yanagi, Y. Yamakawa, Y. Ōno, Phys. Rev. B 81 (2010) 054518.
[32] H. Kontani, S. Onari, Phys. Rev. Lett. 104 (2010) 157001.
[33] Y. Yanagi, Y. Yamakawa, N. Adachi, Y. Ōno, Phys. Rev. B 82 (2010) 064518.
[34] Y. Yanagi, Y. Yamakawa, Y. Ōno, J. Phys. Soc. Jpn. Suppl. C 77 (2008) 149.
[35] Y. Yanagi, Y. Yamakawa, Y. Ōno, Physica C 470 (2010) S349.
[36] J. P. Perdew, K. Burke, M. Ernzerhof, Phys. Rev. Lett. 77 (1996) 3865.
[37] P. Blaha, K. Schwarz, G. Madsen, D. Kvasnicka, J. Luitz, Phys. Rev. Lett. 77 (2002) 3865.
[38] T. Nomura, S. W. Kim, Y. Kamihara, M. Hirano, P. V. Sushko, K. Kato, M. Takata, A. L. Shluger, H. Hosono, Supercond. Sci. Technol. 21 (2008) 125028.
[39] V. Cvetkovic, Z. Tesanovic, Europhys. Lett. 85 (2009) 37002.
[40] C. Cao, P. J. Hirschfeld, H. P. Cheng, Phys. Rev. B 77 (2008) 220506(R).
[41] E. Manousakis, J. Ren, S. Meng, E. Kaxiras, Phys. Rev. B 78 (2008) 205112.
[42] S. Lebegue, Phys. Rev. B 75 (2007) 035110.
[43] D. J. Singh, M. H. Du, Phys. Rev. Lett. 100 (2008) 237003.
[44] K. Haule, J. H. Shim, G. Kotliar, Phys. Rev. Lett. 100 (2008) 226402.
[45] G. Xu, W. Ming, Y. Yao, X. Dai, S.-C. Zhang, Z. Fang, Europhys. Lett. 82 (2008) 67002.
[46] L. Boeri, O. V. Dolgov, A. A. Golubov, Phys. Rev. Lett. 101 (2008) 026403.
[47] H. Tang, M. Plihal, D. Millsh, J. Magn. Magn. Mater. 187 (1998) 23.
[48] T. Takimoto, T. Hotta, K. Ueda, Phys. Rev. B 69 (2004) 104504.
[49] M. Mochizuki, Y. Yanase, M. Ogata, Phys. Rev. Lett. 94 (2005) 147005.
[50] K. Yada, H. Kontani, J. Phys. Soc. Jpn. 74 (2005) 2161.
[51] N. Adachi, Y. Yamakawa, Y. Yanagi, Y. Ōno, in preparation.
[52] T. Moriya, *Spin Fluctuations in Itinerant Electron Magnetism*, Springer,

Berlin, 1985.

[53] The different parameter set of the electron-phonon coupling matrix elements was used in ref. [15], where the transverse d_{yz}-d_{zx} orbital susceptibility shows the incommensurate peaks around $\boldsymbol{q} = (0,0)$ in contrast to the present case. However, the resulting pairing state and the phase diagram was essentially unchanged.

[54] In the present paper, we calculate χ_{O_Γ} at $T < T_c$ as follows. First, we solve the Eliashberg equation at $T = 0.035$ to obtain the gap function $\hat{\Delta}(k)$, where $\lambda = 1.15$. Then, neglecting the ε_n-dependence of the gap function and assuming the usual temperature dependence of the gap function $\hat{\Delta}(\boldsymbol{k}) = \alpha \hat{\Delta}(\boldsymbol{k}, i\pi T_c) \tanh\left(1.74 \sqrt{T_c/T - 1}\right)$, we calculate χ_{O_Γ} at $T < T_c$, where we set $T_c = 0.035$. It is noted that α is determined so as to satisfy the condition $2\Delta_{\max}/k_B T_c = 8$, where $\Delta_{\max}$ is the maximum value of the gap function $\hat{\Delta}(\boldsymbol{k})$ at $T = 0$ on the Fermi surfaces.

[55] K. Hattori, J. Phys. Soc. Jpn. 79 (2010) 114717.

[56] The value of T_0 is determined as follows. First, we fit the experimental results of $(S_{66} - S_{66,0})^{-1}$ for $T > T_c$ at $x = 0.083$ with the function $y = y_0 + aT + bT^2$ to obtain y_0. Then, substituting the obtained y_0 into the SCR equation eq. (A.6), we determine T_0 together with y_1 so as to fit the experimental results of $(S_{66} - S_{66,0})^{-1}$ at $x = 0.083$ with the SCR results as possible.

[57] F. L. Ning, K. Ahilan, T. Imai, A. S. Sefat, M. A. McGuire, B. C. Sales, D. Mandrus, P. Cheng, B. Shen, H.-H. Wen, Phys. Rev. Lett 104 (2010) 037001.

[58] The antiferromagnetic QCP has also been observed in $Ba(Fe_{1-x}Co_x)_2As_2$ at $x \sim 0.065$ [57]. However, the ferro-orbital fluctuation is expected to dominate over the AFM fluctuation for $x \gtrsim x_{QCP} \sim 0.073$.

[59] A. Georges, G. Kotliar, W. Krauth, M. J. Rozenberg, Rev. Mod. Phys 68 (1996) 13.

[60] H. Kusunose, J. Phys. Soc. Jpn. 79 (2010) 094707.

[61] J. H. Chu, J. G. Analytis, K. D. Greve, P. L. McMahon, Z. Islam, Y. Yamamoto, I. R. Fisher, Science 329 (2010) 824.